


Gravity currents in the cabbeling regime

Andrew P. Grace ,* Marek Stastna , and Kevin G. Lamb *Department of Applied Mathematics, University of Waterloo, Waterloo, Ontario N2L 3G1, Canada*K. Andrea Scott *Department of Systems Design Engineering, University of Waterloo, Waterloo, Ontario N2L 3G1, Canada*

(Received 12 August 2022; accepted 9 November 2022; published 5 January 2023)

In this study, we present a series of simulations of gravity currents where ambient and intruding temperatures are on opposite sides of the temperature of maximum density. We use these simulations to describe how cabbeling (mixing of parcels of fluid that leads to a parcel of fluid that is denser) affects the evolution of gravity currents. We show that initially buoyant currents (called hypopycnal currents) undergo mixing in the body and tail region of the gravity current, which generates dense water from cabbeling. We investigate the maximum distance that the initial current progresses as a function of a parameter controlling the nonlinearity of the equation of state (referred to as Θ). We find that the maximum distance that the current progresses is a nonlinear function of Θ . For low Θ hypopycnal currents reverse direction after they begin flowing, and cabbeling occurs over a limited spatial extent. As Θ is increased, currents achieve a larger maximum distance of propagation, allowing the dense water formed by cabbeling to sink and form a secondary current along the bottom of the domain (called a hyperpycnal current). As we increase the parameter controlling the nonlinearity of the equation of state, the hyperpycnal current becomes much larger in scale. We discuss some general characteristics of the hyperpycnal current and highlight that once it forms, larger values of Θ lead to a larger spatial extent of the current but narrower distributions of density and temperature.

DOI: [10.1103/PhysRevFluids.8.014502](https://doi.org/10.1103/PhysRevFluids.8.014502)

I. INTRODUCTION AND OVERVIEW

In recent years physical processes in natural bodies of water during the winter have become very popular to study due to their recognized importance to overall lake health. Powers and Hampton [1] provides a wealth of references on several branches of winter limnology such as the under-ice microbiome, ice phenology, under-ice physical limnology, under-ice primary production, and biogenic gas production and carbon cycling. Recent articles have identified open questions and proposed approaches to solving such problems, some of which cross traditional disciplinary lines [2,3]. Due to the interconnected complexities of under-ice limnology, in this article we are motivated to investigate the impact of an important mechanism known as cabbeling on the development and evolution of a canonical density driven flow known as a gravity current.

In near-surface freshwater, the nonmonotonicity of the nonlinear equation of state (NLEOS) leads to a temperature of maximum density of $\tilde{T}_{md} \approx 3.98^\circ\text{C}$. \tilde{T}_{md} varies with depth due to the temperature dependence of the compressibility of water [4]. However, significant variation from 3.98°C occurs only in very deep bodies of water, such as Lake Baikal. Thus, for most studies focused on shallow fluid systems (such as this one), \tilde{T}_{md} is taken to be constant. For flows with temperatures near \tilde{T}_{md} ,

*andrew.grace@uwaterloo.ca

the nonmonotonicity of the NLEOS also leads to a phenomenon known as cabbelling. In freshwater, cabbelling traditionally occurs when two parcels of equal density but different temperatures mix. If the two parent parcels have temperatures T_1 and T_2 , the child parcel will have a temperature $T_3 = \frac{1}{2}(T_1 + T_2)$, assuming that the parents are of equal mass. However, when $T_1 < \tilde{T}_{md} < T_2$, the density of the child parcel will be greater than the average density of the parent parcels. Cabbelling is especially interesting because the relative density of the child parcel causes it to sink and generate vertical currents (downwelling). Cabbelling also occurs in the ocean because the density of seawater is a function of both the salinity and temperature. Parcels of fluid along the same isopycnal can mix, and this generates denser water that sinks. Several examples of studies concerned with cabbelling in seawater are found in [5–9]. Since the current study is only concerned with freshwater dynamics, the cabbelling due to the presence of salt is intentionally ignored.

As mentioned previously, the impact of cabbelling on a flow known as a gravity current will be investigated within this study. Gravity currents are a canonical example of a horizontal density driven flow, and they are ubiquitous in nature. For example, in the atmosphere, they can manifest themselves as thunderstorm outflows or sea-breeze fronts, both of which are a result of cold and dense air penetrating into a warmer and lighter mass [10,11]. Another example is known as a turbidity current [12]. These appear in both oceans and lakes and can be initiated by sediment-laden river plumes flowing into larger bodies of water, underwater landslides, or even resuspension by intense storms. These kind of currents can travel large distances and are responsible for deposition of sediments along the ocean or lake floor [13]. Depending on their relative density, gravity currents can be positively buoyant (they flow along the upper surface of whatever they are flowing into), they can be negatively buoyant (they sink and flow along the bottom surface), or they can even flow at some middepth if the medium is stably stratified. Finally, due to their inherently simple generation mechanism gravity currents have been extensively studied in both a numerical setting [14–16] and a laboratory setting (Simpson [10,11], Huppert and Simpson [17], Linden *et al.* [18] are some well-known resources). In their mature form, gravity currents represent a state of fluid flow that exhibits the coexistence of coherent structures and turbulence.

In a previous study of gravity currents in cold water, [19] we have investigated the temperature interval between about 1.5 °C and 4 °C over which the density is a strictly increasing, but nonlinear function of temperature. This study described the affect of what was termed “weak cabbelling” (the mixing of two parent parcels of differing density generated a child parcel whose density was greater than the average of the densities of two parent parcels, following Stewart *et al.* [20]) on the development of two classes of gravity currents. The result of which was noticeable differences in the vertical extent and horizontal head location of near-surface flowing gravity currents relative to near-bottom flowing currents for a given magnitude of the initial density difference. In the current study, the characteristic temperature interval is further extended so that the density of freshwater is nonmonotonic. This means that two different water temperatures can now have the same density, with the maximum density occurring at a temperature of \tilde{T}_{md} .

An interesting motivation for the impact of cabbelling on gravity currents in the field occurs during the autumn and spring seasons in intermontane lakes. For instance, measurements taken from Kamloops Lake (Canada) in Carmack [21], Carmack *et al.* [22] indicate that the lake undergoes several distinct circulation patterns throughout the year due to the inflowing Thompson River at the east end of the lake. These circulation patterns are driven by the relative temperature differences of the lake and the river waters. Specifically, observations presented in Carmack *et al.* [22] show that in the late spring when river water is greater than 4 °C, river water flows out along the surface of the lake, but due to the cabbelling instability, a river-lake mixture becomes locally denser leading to a density driven current that plunges to the bottom of the lake. If this interaction occurs above a slope, the dense fluid formed by cabbelling can flow several kilometers to deeper regions in the lake. Due to this mechanism, the lake fills with warm water from the bottom up.

In some instances, this can lead to a related phenomenon known as thermal bar circulation, which occurs when a warm mass of water with temperatures greater than 4 °C in a shallow

region is adjacent to a mass of water with temperatures less than 4°C . In this instance, a wedge forms that effectively traps riverine inflow water [21]. Carmack [21] showed measurements of a thermal bar induced by the Thompson River inflow in the late spring in Kamloops Lake. Measurements indicate that these thermal bars can extend several hundred meters lakeward and to depths of tens of meters in the near-shore regions. This trapping effect by the thermal bar means that all water reaching the outflow at the west end of the lake must come from the surface waters, and with it comes whatever properties it possessed from the preceding winter. Thus, thermal bars and the associated circulation patterns may have significant ecological implications, as well as impacting pollutant transport in lakes. Since horizontal currents typically cannot penetrate the thermal bar, there is limited horizontal mixing which compounds eutrophication problems in near-shore regions [23]. Additionally, the thermal bar was historically thought to be a mechanism responsible for deep water renewal in Lake Baikal [24], but other mechanisms have since been proposed [25]. A more vigorous example of cabbeling may be found near a nuclear power plant outflow during the winter. Nuclear power plants adjacent to lakes use ambient water for cooling purposes. In most instances the used water discharged leading to a plume of significantly higher temperatures relative to the cold ambient. When the warmer water is expelled into the cold ambient, it is initially less dense and will float. However, as the warm water mass mixes with the ambient water, it becomes denser and sinks, and may stay in the hypolimnion potentially altering the mixing regime of the lake itself [26]. Gaudard *et al.* [27] reviews some of the impacts of significant thermal discharge on physical and ecological processes in lakes and rivers.

Large-scale cabbeling is difficult to study at high resolution with direct numerical simulations due to the characteristic length scales required to study it. As an example in a simulation context, consider the work of Tsydenov *et al.* [28] who conducted 2.5D (three spatial dimensions, but gradients cannot form in the spanwise dimension) numerical simulations of the thermal bar in a model for a deep lake. Their Fig. 4 highlights the main process discussed above. The domain used in their study models the near-shore regions of Lake Baikal and as such covers 10 km in the cross-isobath direction and 300 m in depth. Thus, the scales of this phenomenon require the use of turbulence models to estimate the subgrid scale turbulence and the diffusion of mean quantities. Tsydenov *et al.* [28] used the two-parameter k - ϵ model of Wilcox [29] to compute the vertical diffusivity, while also using a constant horizontal value. The k - ϵ model is useful in many contexts as it is simple. However, its performance has been known to suffer in complex flows (though the term “complex” is not exactly precise in this context) [30]. As another example, Holland *et al.* [31] used a diffusivity that was inversely proportional to the local buoyancy frequency above some small cutoff. Below this cutoff, a constant diffusivity four orders of magnitude greater than the molecular value was chosen. As with any empirical model, this turbulence model can be tuned to fit the specific context, but the model is phenomenological in nature. In the present study, the difficulty of selecting an appropriate turbulence model, and tuning it, is side-stepped by instead performing small scale direct numerical simulations (DNS).

In this study, we present simulations of the evolution of gravity currents where temperatures of the intrusion and the ambient are on opposite sides of \tilde{T}_{md} , leading to cabbeling. The addition of the cabbeling mechanism in this context leads to some interesting and emergent dynamics. We will demonstrate that gravity currents initially flow near the top surface of the domain (i.e., take the form of a hypopycnal current), undergo cabbeling induced by mixing, and develop coherent currents that flow near the bottom boundary (i.e., take the form of a hyperpycnal current). While the mechanism presented within this paper is different, the behavior is reminiscent of a process known as convective sedimentation below buoyant hypopycnal flows [12]. We analyze the impact of parameters known as the NLEOS parameter Θ and the nondimensional depth of the system h (both to be defined below) on the development of the initial hypopycnal current, and its transition to the hyperpycnal current. We will demonstrate that these parameters play an important role in determining the characteristics of the secondary hyperpycnal current, and discuss the implications for the study of the secondary hyperpycnal currents.

TABLE I. The list of constant parameters used in this study, their values, dimensions, and a description.

Parameter Symbol	Value	Dimensions	Description
g	9.81	m/s ²	Acceleration due to gravity
\tilde{T}_{md}	3.98	°C	Temperature of maximum density
ρ_0	999.974	kg/m ³	Constant reference density
C	7.6×10^{-6}	°C ⁻²	NLEOS constant [see (1)]
H	2	m	Dimensional depth of domain
L	20	m	Dimensional length of domain
Pr	10	–	Prandtl number [see (14)]
x_ℓ	8	–	Dimensionless lock length

II. GOVERNING EQUATIONS AND MODEL SETUP

This study presents an extension of the work in Grace *et al.* [19] into the cabbeling regime, where the density of water can be nonmonotonic (different values of temperature can correspond to the same density). We use SPINS [32] to solve the incompressible Navier-Stokes equations under the Boussinesq approximation in order to investigate the evolution of gravity currents with a characteristic temperature and density of \tilde{T}_i and $\rho(\tilde{T}_i)$ and height of z_0 propagating into a motionless ambient of temperature and density \tilde{T}_a and $\rho(\tilde{T}_a)$ in freshwater in two dimensions. In this study, the intruding and ambient temperatures are on different sides of the temperature of maximum density. The boundary conditions along all surfaces are free-slip for velocity, and no-flux for temperature, and the model achieves spectral accuracy. The motivation of free-slip boundary conditions is as follows. First, in the laboratory experiments of convective sedimentation by Sutherland *et al.* [33] and Davarpanah Jazi and Wells [34], sediment laden gravity currents initially flowed along the free surface (on top of the saline ambient). The evolution of sediment-laden gravity currents could be considered an analog to the gravity currents presented in this study. Additionally, for a buoyant surface current initiating a thermal bar at the field scale, the surface boundary condition is very complicated due to a variety of factors such as thermal boundary layers, variable ice roughness, wind, and surface waves. Since we are taking a simplified approach in our investigation of this system, we are not interested in effects by the boundary layer and are only interested in interior mixing, thus motivating the simple boundary conditions. In this study the dimensional length of the domain is $L = 20$ m (Table I), and the depth is kept constant at $H = 0.5$ m (Table I). All simulations presented have 8192 uniformly spaced grid points in the horizontal dimension and 256 uniformly spaced grid points in the vertical direction, leading to a physical resolution of $(\Delta x, \Delta z) = (0.0024, 0.0020)$ m. A resolution sensitivity test was performed and the chosen resolution is adequate to represent the system. In this study, variables with a tilde are dimensional quantities.

In this study the departure of density from a reference state ρ_0 (Table I) is

$$\rho = -C(\tilde{T} - \tilde{T}_{md})^2. \quad (1)$$

This equation differs from Grace *et al.* [19] where the NLEOS was cubic. The choice to use the quadratic EOS is motivated by the fact it is simpler and has fewer dimensional parameters than its cubic counterpart. This quadratic EOS has been used in several recent studies [35,36]. (1) contains the temperature of maximum density \tilde{T}_{md} and constant C (both found in Table I) as parameters. Also note that ρ in (1) is already dimensionless.

The temperature field is scaled as

$$T = \frac{\tilde{T} - \tilde{T}_a}{\Delta \tilde{T}_1} \quad (2)$$

with $\Delta \tilde{T}_1 = \tilde{T}_i - \tilde{T}_a$. This scaling is motivated by the usual temperature (or density) scaling for gravity currents. By choosing this scaling, T varies between 0 and 1, where $T = 0$ corresponds

to the ambient temperature and $T = 1$ corresponds to the intrusion temperature. Alternatively, we could have chosen to scale the temperature field relative to \tilde{T}_{md} instead of \tilde{T}_a . Ultimately, this choice will not have an impact on the main results of the paper. We have included the subscript in the definition for $\Delta\tilde{T}_1$ because, as we shall see, this is not the only temperature scale that we must define. We can use the above nondimensional temperature to nondimensionalize the density

$$\rho = -C[\Delta\tilde{T}_1 T - (\tilde{T}_{md} - \tilde{T}_a)]^2, \quad (3)$$

where we can define $\Delta\tilde{T}_2 = \tilde{T}_{md} - \tilde{T}_a$ and the NLEOS parameter as

$$\Theta = \frac{\Delta\tilde{T}_1}{\Delta\tilde{T}_2} = \frac{\tilde{T}_i - \tilde{T}_a}{\tilde{T}_{md} - \tilde{T}_a}. \quad (4)$$

This parameter was discussed in the work of Carmack [21] in the context of production rate of 4 °C water as a result of mixing of river and lake water in Kamloops Lake. Note that the nondimensional temperature of maximum density is given by $\frac{1}{\Theta}$. Note also that if we had chosen to scale the temperature field relative to \tilde{T}_{md} , the definition of Θ would instead be

$$\Theta_r = \frac{\tilde{T}_i - \tilde{T}_{md}}{\tilde{T}_a - \tilde{T}_{md}}. \quad (5)$$

Again, the results of this paper would be unchanged by using Θ_r instead of Θ as a controlling parameter. It is also easy to show that

$$\Theta = 1 - \Theta_r. \quad (6)$$

Expanding (3), and noting that $\tilde{\rho}(\tilde{T}_a) = -C(\Delta\tilde{T}_2)^2$, we can write the nondimensional NLEOS as

$$\rho = \rho(\tilde{T}_a) + 2C\Theta(\Delta\tilde{T}_2)^2 T \left(1 - \frac{\Theta}{2} T\right). \quad (7)$$

We can define the buoyancy velocity scale and timescale as

$$U_b = \sqrt{g'z_0}, \quad t_b = \sqrt{\frac{z_0}{g'}}, \quad (8)$$

where $g' = g|\rho(\tilde{T}_i) - \rho(\tilde{T}_a)|$ is the reduced gravity, and z_0 is the initial height of the intruding fluid (Table II).

We can simplify the reduced gravity to

$$g|\rho(\tilde{T}_i) - \rho(\tilde{T}_a)| = Cg|\Theta(\Theta - 2)|(\Delta\tilde{T}_2)^2, \quad (9)$$

allowing us to write

$$U_b = \sqrt{Cg|\Theta(\Theta - 2)|(\Delta\tilde{T}_2)^2 z_0}. \quad (10)$$

Using these scales, we can nondimensionalize the system as

$$(x, z) = \frac{(\tilde{x}, \tilde{z})}{z_0}, \quad (u, w) = \frac{(\tilde{u}, \tilde{w})}{U_b}, \quad t = \tilde{t} \sqrt{\frac{g'}{z_0}}, \quad p = \frac{\tilde{p}}{\rho_0 U_b^2}. \quad (11)$$

In this study, the form of initial condition can accommodate different values for height of the initial hypopycnal current z_0 . In nondimensional form, the initial condition for the system is

$$T(x, z, t = 0) = \frac{\mathcal{B}(z)}{2} \left[1 - \tanh\left(\frac{x - x_\ell}{\delta_x}\right) \right], \quad (12)$$

TABLE II. The cases presented in this study. Case names are denoted by the “Txxhyy,” where xx and yy represent the value of Θ [the NLEOS parameter (4)] and h (the depth of the domain, found in the rightmost column) for the case. The exception to this are cases preceded by a “V.” In those instances, the viscosity and thermal diffusivity have been reduced by 50%. Gr represents the Grashof number, (14), \tilde{T}_i is the dimensional intruding temperature, \tilde{T}_a is the dimensional ambient temperature, and ν is the kinematic viscosity. Parameters that remain unchanged in groups of cases are shown in the rightmost column. δ_x and δ_z are the transition thicknesses in the x and z directions, respectively, and l is the tank length.

Case	Gr	Θ	\tilde{T}_i ($^{\circ}\text{C}$)	\tilde{T}_a ($^{\circ}\text{C}$)	$10^6\nu$ (m^2/s)	
T2.2h4	1.43×10^5	2.2	2.156	5.5	1	$\delta_x = 0.8, \delta_z = 0.08$ $h = 4, l = 160$
T3h4	1.00×10^6	3.0	0.944	5.5	1	
T4h4	2.68×10^6	4.0	8.5	2.5	1	
T5h4	4.82×10^6	5.0	9.9	2.5	1	
T6h4	7.71×10^6	6.0	11.38	2.5	1	
VT5h4	1.93×10^7	5.0	9.9	2.5	0.5	
VT6h4	3.08×10^7	6.0	11.38	2.5	0.5	
T7h4	1.12×10^7	7.0	12.86	2.5	1	
T8h4	1.59×10^7	8.0	14.5	2.5	1	
T2.2h2	1.14×10^6	2.2	2.156	5.5	1	$\delta_x = 0.4, \delta_z = 0.04$ $h = 2, l = 80$
T2.4h2	2.55×10^6	2.4	1.852	5.5	1	
T2.63h2	4.44×10^6	2.63	1.500	5.5	1	
T2.8h2	6.00×10^6	2.8	1.244	5.5	1	
T3h2	8.03×10^6	3.0	0.944	5.5	1	
T3.5h2	1.56×10^7	3.5	0.018	5.5	1	
T4h2	2.14×10^7	4.0	8.5	2.5	1	
T5h2	3.86×10^7	5.0	9.9	2.5	1	
T6h2	6.17×10^7	6.0	11.38	2.5	1	
T7h2	9.00×10^7	7.0	12.86	2.5	1	
T8h2	1.27×10^8	8.0	14.5	2.5	1	
T3h1.82	1.07×10^7	3.0	0.944	5.5	1	$\delta_x = 0.365, \delta_z = 0.0364$ $h = 1.82, l = 72.7$
T4h1.82	2.86×10^7	4.0	8.5	2.5	1	
T5h1.82	5.14×10^7	5.0	9.9	2.5	1	
T6h1.82	8.21×10^7	6.0	11.38	2.5	1	
T7h1.82	1.20×10^8	7.0	12.86	2.5	1	
T8h1.82	1.69×10^8	8.0	14.5	2.5	1	

where \mathcal{B} is defined as

$$\mathcal{B}(z) = \frac{1}{2} \left[1 + \beta \tanh \left(\frac{z-1}{\delta_z} \right) \right]. \quad (13)$$

\mathcal{B} allows us to select the initial height of the intruding fluid relative to the top surface ($\beta = 1$) or the bottom surface ($\beta = -1$). The parameters δ_x and δ_z are the dimensionless transition thicknesses, while x_ℓ (Table I) is the dimensionless lock length. Since all lengths in the problem are scales relative to z_0 , the initial intrusion height sets the reference length scale. This is illustrated in Fig. 1. The domain depth and length are also normalized by the intrusion height. They are $h = H/z_0$ and $l = L/z_0$ and their values are found in Table II. Note that while x_ℓ remains constant for all simulations, the dimensional lock length $x'_\ell = x_\ell z_0$, or alternatively, $x'_\ell = x_\ell H/h$. A schematic of the initial condition is provided in Fig. 1.

We can define the Grashof number and the Prandtl number as

$$\text{Gr} = \left(\frac{U_b z_0}{\nu} \right)^2, \quad \text{Pr} = \frac{\nu}{\kappa}, \quad (14)$$

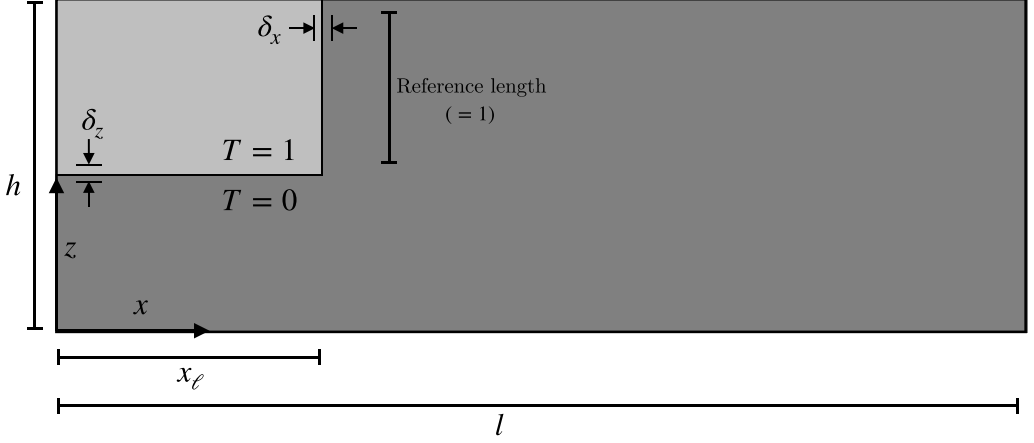


FIG. 1. A schematic of the initial condition demonstrating the initial locations of the intrusion and ambient, which are defined to have temperatures of one and zero respectively. In all cases, the intrusion is initially located adjacent to the top left corner of the domain. The initial hypopycnal current depth is varied across cases. The lock length is given by x_ℓ , the tank length given by l , and the tank depth given by h . x is the horizontal coordinate, and z is the vertical coordinate, and gravity points in the negative z direction. Lengths are nondimensionalized by z_0 , so the initial intrusion height serves as the reference length.

which give the equations of motion as

$$\frac{D\mathbf{u}}{Dt} = -\nabla p - \frac{2}{\Theta - 2} T \left(1 - \frac{\Theta}{2} T \right) \hat{\mathbf{k}} + \frac{1}{\sqrt{\text{Gr}}} \nabla^2 \mathbf{u}, \quad (15)$$

$$\frac{DT}{Dt} = \frac{1}{\sqrt{\text{GrPr}^2}} \nabla^2 T, \quad (16)$$

$$\nabla \cdot \mathbf{u} = 0. \quad (17)$$

Here we can see that Θ controls the relative magnitude of the nonlinear term in (15), except in this case, and can attain a large range of values set by the initial conditions \tilde{T}_i and \tilde{T}_a . Note that $\Theta = 2$ leads to the case where $U_b = 0$, and there is no longer a buoyancy velocity to scale by. $\Theta = 2$ is special case that must be discussed separately and is done so as a part of the following section.

A. Gravity current classification based on initial intruding and ambient temperatures

Assuming $\Delta\tilde{T}_1 > 0$ ($\tilde{T}_i > \tilde{T}_a$) we can build a framework for the classification of gravity currents based on their Θ value. Note that because of the symmetry of the NLEOS about \tilde{T}_{md} , a dynamically equivalent classification can be developed for the case where $\Delta\tilde{T}_1 < 0$ ($\tilde{T}_i < \tilde{T}_a$) using the map $\tilde{T}_i \rightarrow 2\tilde{T}_{md} - \tilde{T}_i$ and $\tilde{T}_a \rightarrow 2\tilde{T}_{md} - \tilde{T}_a$. Furthermore, an exact NLEOS is slightly asymmetric about \tilde{T}_{md} , so currents with $\Delta\tilde{T}_1 < 0$ will not evolve exactly as those with $\Delta\tilde{T}_1 > 0$. This is of no consequence for this study because the exact NLEOS is not used here, and differences are expected to be small.

In the following section, we will consider eight different cases: $\Theta = 1$, $\Theta = -1$, $\Theta < -1$, $\Theta \in (-1, 0^-)$, $\Theta \in (0^+, 1)$, and $\Theta \in (1, 2)$, $\Theta = 2$, and $\Theta > 2$. With this information, we can determine the relative ordering of the intruding temperature, ambient temperature, and temperature of maximum density, and discuss the expected evolution characteristics. The following section goes through each case, but for readers simply interested in a summary, see Fig. 2 and Table III. As a reminder, the NLEOS parameter is defined as

$$\Theta = \frac{\Delta\tilde{T}_1}{\Delta\tilde{T}_2} = \frac{\tilde{T}_i - \tilde{T}_a}{\tilde{T}_{md} - \tilde{T}_a}. \quad (18)$$

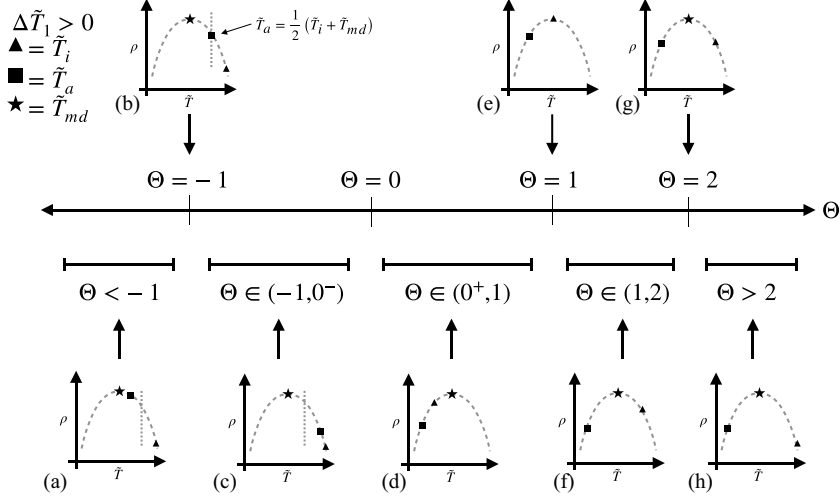


FIG. 2. A schematic representation of different values and intervals of Θ and what they imply about the expected behavior of the resulting gravity current. Each set of axes shows the quadratic equation of state and the markers represent the temperatures of the intruding fluid (triangles) and the ambient fluid (squares), as well as the temperature of maximum density (stars). It is assumed that $\Delta\tilde{T}_1 > 0$. For cases where $\Delta\tilde{T}_1 < 0$ is of equal magnitude and opposite sign, the location of the temperature markers are flipped across the line $\tilde{T} = \tilde{T}_{md}$. Dotted vertical lines represent the average of the intruding and ambient temperatures and are included only where necessary.

I. $\Theta < -1$

For the case where $\Theta < -1$, $\Delta\tilde{T}_1$ and $\Delta\tilde{T}_2$ must have opposite sign, so when $\Delta\tilde{T}_1 > 0$ and $\Delta\tilde{T}_2 < 0$, we find that

$$\tilde{T}_a < \frac{\tilde{T}_i + \tilde{T}_{md}}{2} \quad (19)$$

and

$$\tilde{T}_i > \tilde{T}_a > \tilde{T}_{md}. \quad (20)$$

TABLE III. A representation of the ordering the intruding temperature, ambient temperature, and temperature of maximum density (\tilde{T}_i , \tilde{T}_a , and \tilde{T}_{md} , respectively) given different intervals of Θ for positive $\Delta\tilde{T}_1$. Θ is defined in (4) and $\Delta\tilde{T}_1 = \tilde{T}_i - \tilde{T}_a$.

Case	Ordering of \tilde{T}_i , \tilde{T}_a , and \tilde{T}_{md}
$\Theta < -1$	$\tilde{T}_i > \tilde{T}_a > \tilde{T}_{md}$ and $\tilde{T}_a < \frac{1}{2}(\tilde{T}_i + \tilde{T}_{md})$
$\Theta = -1$	$\tilde{T}_i > \tilde{T}_a > \tilde{T}_{md}$ and $\tilde{T}_a = \frac{1}{2}(\tilde{T}_i + \tilde{T}_{md})$
$-1 < \Theta < 0$	$\tilde{T}_i > \tilde{T}_a > \tilde{T}_{md}$ and $\tilde{T}_a > \frac{1}{2}(\tilde{T}_i + \tilde{T}_{md})$
$1 > \Theta > 0$	$\tilde{T}_a < \tilde{T}_i < \tilde{T}_{md}$
$\Theta = 1$	$\tilde{T}_i = \tilde{T}_{md}$
$1 < \Theta < 2$	$\frac{1}{2}(\tilde{T}_i + \tilde{T}_a) < \tilde{T}_{md}$
$\Theta = 2$	$\frac{1}{2}(\tilde{T}_i + \tilde{T}_a) = \tilde{T}_{md}$
$\Theta > 2$	$\frac{1}{2}(\tilde{T}_i + \tilde{T}_a) > \tilde{T}_{md}$

We can see that this interval of Θ implies that \tilde{T}_a is always closer to \tilde{T}_{md} than it is to the \tilde{T}_i . Therefore, as Θ gets more negative, \tilde{T}_a approaches \tilde{T}_{md} . Note that this critical value was that which characterized the T cases in Grace *et al.* [19]. This regime is presented in Fig. 2(a).

2. $\Theta = -1$

In this case $\Delta\tilde{T}_1$ and $\Delta\tilde{T}_2$ must be equal in absolute value but opposite in sign. In this case

$$\tilde{T}_a = \frac{\tilde{T}_i + \tilde{T}_{md}}{2} \quad (21)$$

and

$$\tilde{T}_i > \tilde{T}_a > \tilde{T}_{md} \quad (22)$$

must be true. This indicates, that for $\Theta = -1$, \tilde{T}_i and \tilde{T}_a are both greater than \tilde{T}_{md} and that \tilde{T}_a must be the average of \tilde{T}_i and \tilde{T}_{md} . This case is illustrated in Fig. 2(b). The average of \tilde{T}_i and \tilde{T}_{md} is highlighted by a dotted vertical line.

3. $\Theta \in (-1, 0^-)$

In the case $\Theta \in (-1, 0^-)$, $\Delta\tilde{T}_1$ and $\Delta\tilde{T}_2$ must have the opposite sign but $\Delta\tilde{T}_1$ must be smaller in absolute value than $\Delta\tilde{T}_2$. In this case

$$\tilde{T}_a > \frac{\tilde{T}_i + \tilde{T}_{md}}{2}. \quad (23)$$

Thus, \tilde{T}_a must be greater than the average of \tilde{T}_i and \tilde{T}_{md} . Additionally, since $\Delta\tilde{T}_1 > 0$ and $\Delta\tilde{T}_2 < 0$, we must have

$$\tilde{T}_i > \tilde{T}_a > \tilde{T}_{md}. \quad (24)$$

We can see that as \tilde{T}_a becomes larger than $\frac{\tilde{T}_i + \tilde{T}_{md}}{2}$, the characteristic temperatures of the gravity current tend to move further away from the nonlinearity of the NLEOS. Thus, as $\Theta \rightarrow 0^-$, one expects the nonlinear term in the NLEOS to become smaller in magnitude relative to the linear term. This case is illustrated in Fig. 2(c).

4. $\Theta \in (0^+, 1)$

In the interval $\Theta \in (0^+, 1)$, $\Delta\tilde{T}_1$ and $\Delta\tilde{T}_2$ must have the same sign, but $\Delta\tilde{T}_1 < \Delta\tilde{T}_2$. It follows that

$$\tilde{T}_a < \tilde{T}_i < \tilde{T}_{md}. \quad (25)$$

Thus, for values $\Theta \in (0^+, 1)$ we have that the intruding temperature is between the temperature of maximum density and the ambient temperatures. In this case, the intrusion is denser than the ambient, so the current will sink. This case is illustrated in Fig. 2(d).

5. $\Theta = 1$

In this case, $\Delta\tilde{T}_1$ and $\Delta\tilde{T}_2$ must be equal. The only ordering that allows for this is to have $\tilde{T}_i = \tilde{T}_{md}$. Thus, for $\Theta = 1$, the only gravity current class that can exist is one where the intruding fluid is at the temperature of maximum density. In this case, the intrusion is maximally dense, so it sinks. Note that this critical value was that which characterized the B cases in Grace *et al.* [19]. This case is illustrated in Fig. 2(e).

6. $\Theta > 1$

For the case of $\Theta > 1$, $\Delta\tilde{T}_1$ and $\Delta\tilde{T}_2$ have to be of the same sign and $\Delta\tilde{T}_1 > \Delta\tilde{T}_2$. The ordering then becomes

$$\tilde{T}_i > \tilde{T}_{md} > \tilde{T}_a. \quad (26)$$

Thus, the ambient temperature must be less than the temperature of maximum density, while the intruding temperature must be higher. This regime is important because mixing of two parent parcels of fluid generates a parcel that is heavier and sinks. The results dynamics in this interval can be further subdivided into two subintervals $\Theta \in (1, 2)$ and $\Theta > 2$. For $\Theta \in (1, 2)$, the density of the intrusion is higher than the ambient, so the intrusion initially sinks. However, as the intrusion and the ambient mix, they form denser water, which in turn has a larger density difference relative to the ambient than the intrusion. Thus, as mixing occurs, a faster moving current may form. For Θ in this interval, it can be shown that

$$\tilde{T}_{md} < \frac{\tilde{T}_i + \tilde{T}_a}{2}. \quad (27)$$

In-depth analysis of $\Theta \in (1, 2)$ is left for future work. This case is illustrated in Fig. 2(f).

If $\Theta = 2$, then the ambient and intruding densities are the same. In terms of \tilde{T}_i , \tilde{T}_a , and \tilde{T}_{md} , we must have

$$\tilde{T}_{md} = \frac{\tilde{T}_i + \tilde{T}_a}{2}. \quad (28)$$

In this case, there is no initial collapse and no horizontal intrusion is generated. There is mixing along the interface between the two masses of water that generate vertical currents. This observation is consistent with the scaling U_b , which showed that the current speed would be zero in the event of $\Theta = 2$. In this event, a different velocity scaling should be used. This case is illustrated in Fig. 2(g).

If $\Theta > 2$, then

$$\tilde{T}_{md} < \frac{\tilde{T}_i + \tilde{T}_a}{2}. \quad (29)$$

In this case, the intruding density is initially lower than the ambient (save for a band of dense water surrounding the initial mass of water), thereby allowing the current to initially rise to the top boundary. As the intrusion propagates and mixes with the ambient water, dense water is created which sinks. The $\Theta > 2$ regime is fascinating and will be the focus of the rest of this study. In the following sections, we will discuss the dynamics of the $\Theta > 2$ regime specifically highlighting the dynamics as Θ is increased beyond two. This case is illustrated in Fig. 2(h).

An interesting result occurs in the limit of large Θ . Using dimensionless variables now, we can rewrite the buoyancy forcing term in (15) as

$$\rho = -\frac{2}{1 - \frac{2}{\Theta}} T \left(\frac{1}{\Theta} - \frac{T}{2} \right). \quad (30)$$

Letting $\epsilon = \frac{1}{\Theta}$, we arrive at

$$\rho = -\frac{2}{1 - 2\epsilon} T \left(\epsilon - \frac{T}{2} \right). \quad (31)$$

In the limit of large Θ (or small ϵ), we can expand the temperature as

$$T = T^{(0)} + \epsilon T^{(1)} + O(\epsilon^2), \quad (32)$$

and substituting (32) into (31), we find that

$$\rho \approx (T^{(0)})^2 - 2\epsilon[(T^{(0)})^2 - T^{(0)}(1 - T^{(1)})] + O(\epsilon^2). \quad (33)$$

Expressing the density as an expansion in ϵ as $\rho = \rho^{(0)} + \epsilon\rho^{(1)} + O(\epsilon^2)$, we find that

$$\rho^{(0)} = (T^{(0)})^2, \quad (34)$$

$$\rho^{(1)} = 2(T^{(0)})^2 - 2T^{(0)}(1 - T^{(1)}), \quad (35)$$

meaning that $\rho^{(0)}$ is a monotonic function of $T^{(0)}$. Since the density is monotonic at leading order, cabbling becomes a higher order effect (recall that cabbling occurs because of the nonmonotonic nature of the NLEOS). Ignoring terms of $O(\epsilon^2)$ and higher, we are left with an equation of state that is quadratic (but monotonic) in $T^{(0)}$ and linear in $T^{(1)}$. Thus, for $\Theta > 2$ cabbling occurs until $\epsilon = \frac{1}{\Theta}$ becomes small, at which point, cabbling becomes a secondary effect and the leading order effect is to evolve under a monotonic NLEOS, specifically one that is purely quadratic in temperature. This means that gravity currents with large values of Θ evolve similarly to the near-surface currents discussed in Grace *et al.* [19] (called the T cases) to leading order.

Figure 2 and Table III are provided as visual summaries of the above discussion. In Fig. 2, it is assumed that $\Delta\tilde{T}_1 > 0$ for brevity. For cases where $\Delta\tilde{T}_1 < 0$ the locations of each marker on the diagram would be reflected about \tilde{T}_{md} .

B. Experimental configuration

To discuss the physics of the $\Theta > 2$ regime, we will present two experiments. We must have $\frac{1}{2}(\tilde{T}_i + \tilde{T}_a) > \tilde{T}_{md}$ to ensure that $\Theta > 2$. In this study \tilde{T}_a is either 2.5 °C or 5.5 °C. However, $\Delta\tilde{T}_2^2$ does not change between cases (see Table II for details). In the first experiment, Θ is manipulated by varying the magnitude of $\Delta\tilde{T}_1$. In the second experiment, the relative intrusion depth is manipulated by varying the total depth of the domain h . By modifying h , we are modifying the amount of intruding fluid relative to the domain depth, which leads to variations in the head height of the initial hypopycnal current. For gravity currents under linear equations of state, the head height of the current is about half the height of the initial intrusion (for large enough Grashof number; for smaller Grashof numbers, viscosity plays a more prominent role in determining the characteristics of the resulting current). Cases are presented in Table II and are named based on their values for Θ and h . See the caption of Table II for details.

Note that by changing Θ and h , we also change the Grashof number. This motivates the definition of another number called Gr_0 . It is defined as

$$\text{Gr}_0 = \frac{gC(\Delta\tilde{T}_2)^2H^3}{\nu^2}. \quad (36)$$

Since the magnitude of $\Delta\tilde{T}_2$ is held constant in this study, Gr_0 is invariant upon changing Θ or h . The Grashof number in Table II is related to Gr_0 by

$$\text{Gr} = \text{Gr}_0 \frac{\Theta}{h^3}. \quad (37)$$

Gr_0 is held constant for all cases except VT5h4 and VT6h4 where it has been increased by a factor of four.

III. RESULTS

A. Θ and h dependence of the development of the flow

In this subsection, the results of several numerical simulations in the $\Theta > 2$ regime will be shown. To discuss the basic dynamics, we can consider T3h2, which has $\Theta = 3$ and $h = 2$. Neither Θ nor h is an extreme value considered in this study, and so cabbling is still a leading order effect ($\epsilon = \frac{1}{\Theta}$ is not small compared to unity). Snapshots of the temperature and velocity fields at different times for T3h2 case are shown in Figs. 3 and 4, respectively. The dynamics of the other cases for each experiment are qualitatively similar, with only minor differences in the details.

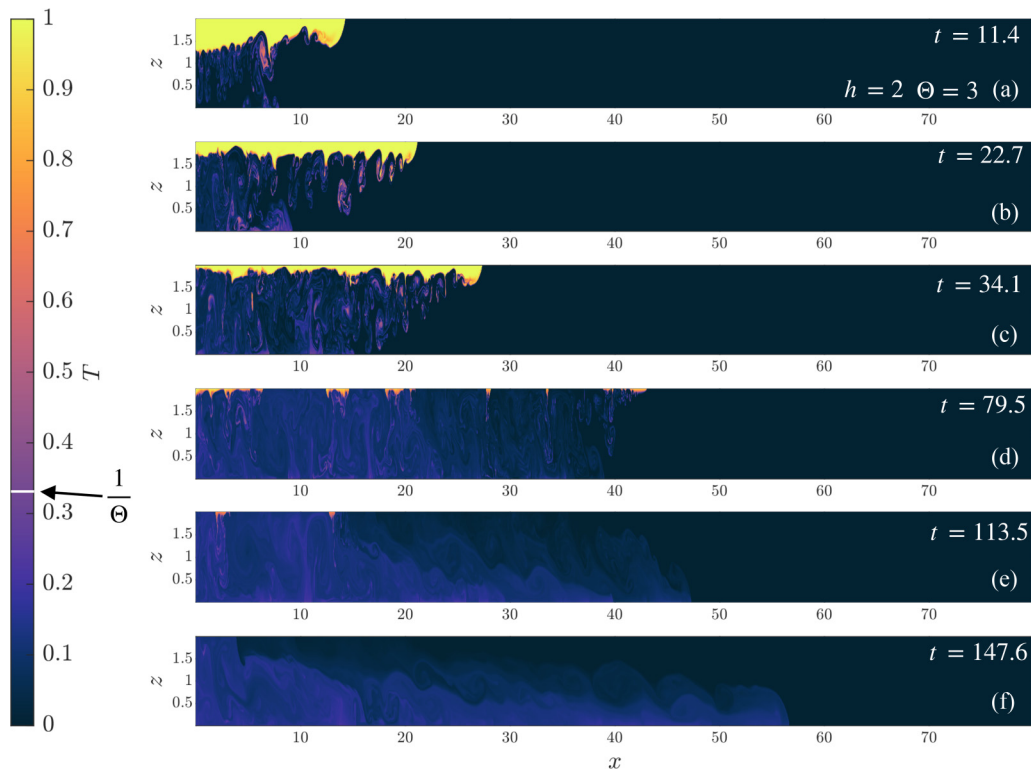


FIG. 3. Temperature fields for T3h2, given by (2). The nondimensional temperature of maximum density for T3h2 ($\frac{1}{\Theta}$) is marked on the colorbar. Times are located on each panel. Panels (a)–(c) show the general evolution of the hypopycnal (near-surface) current, panel (d) shows a transition time, and panels (e) and (f) show the hyperpycnal (near-bottom) current. Notice the increase in head height in panel (f) relative to panel (a). Notice also that the hyperpycnal current quickly outruns the hypopycnal current.

Figure 3 shows that the initial hypopycnal current, which is lighter than the ambient (except for a thin band around the intrusion), flows from left to right along the top surface. Mixing in the body and tail of the current creates water of a higher density than both the intrusion and the surrounding ambient. The denser fluid sinks, as visible in Figs. 3(a)–3(c). We can see that the initial intruding water mass quickly mixes due to this process. Once enough dense fluid gathers near the bottom surface, a new coherent hyperpycnal current is created. This current flows away from the left wall, visible in Figs. 3(d)–3(f). Due to the propagation of the hyperpycnal current, a near-surface reverse flow is induced which pushes the remains of the initial hypopycnal current back towards the left-hand wall.

The hyperpycnal current has a new typical temperature and is heavier than the ambient, thus allowing it to flow along the bottom. Qualitatively speaking, the volume of the hyperpycnal current is much larger than the initial hypopycnal current indicating that a significant volume of ambient water has been entrained over the course of the cabbelling process. Note the time jump between panels (c) and (d). Recall that the nondimensional temperature of maximum density is given by $1/\Theta$ (approximately $1/3$ in this case), and it is important to note that the temperature of the bottom current is lower than $1/\Theta$, indicating that the hyperpycnal current consists of fluid that is not simply the maximally dense fluid, but some other temperature whose value is an emergent quantity of the dynamical process. This is true for all cases discussed in this study, and a more detailed discussion on the temperatures of the bottom currents is presented below.

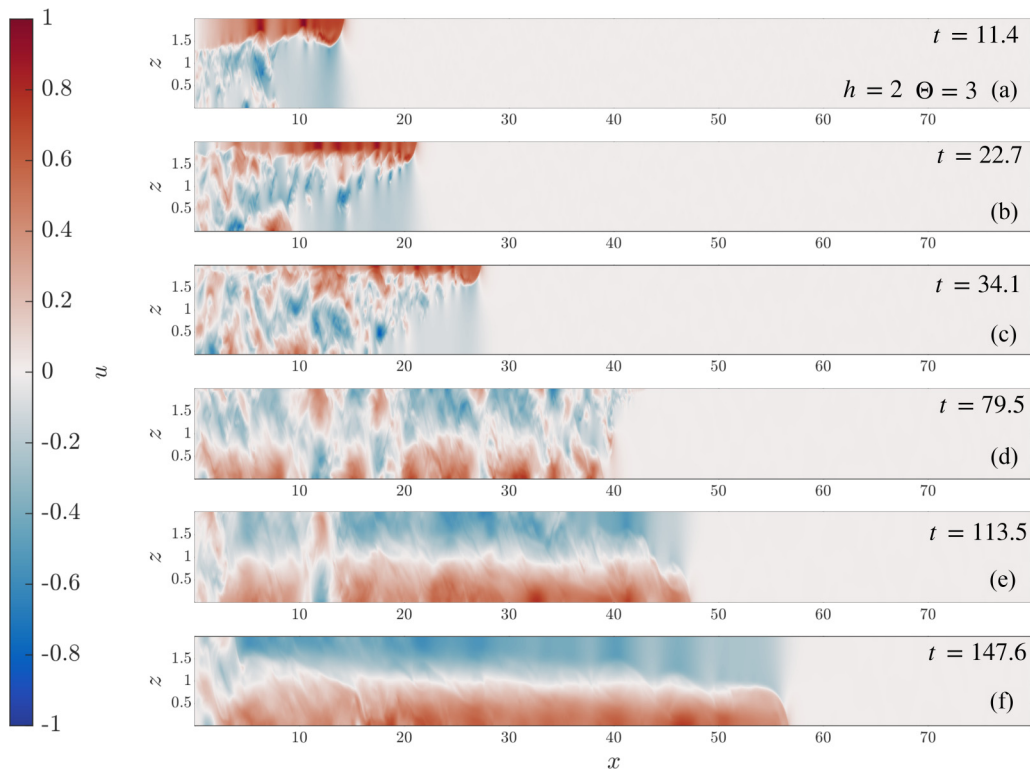


FIG. 4. Horizontal component of nondimensional flow velocity for T3h2. The times of each plot are the same as in Fig. 3. Notice the decrease in the velocity of the current in panel (f) relative to panel (a).

Figure 4 shows the dimensionless horizontal component of the velocity field. The initial hypopycnal current develops and flows along the top surface [Figs. 4(a)–4(c)]. The currents shown in Fig. 4(d) are very irregular, but this state is ultimately a transition between the hypopycnal and hyperpycnal currents. In Figs. 4(e) and 4(f), we can see the signature of the hyperpycnal as it propagates to the right, and the return flow moving to the left near the top surface. It is interesting to note that the head height of the bottom current is approximately half the depth of the domain, which is in qualitative agreement to that seen in the full-depth lock release simulations from both Härtel *et al.* [15] and Cantero *et al.* [37] in the slumping regime. Furthermore, we can see that the velocities in the hyperpycnal current are weaker than those in the hypopycnal current. The transition from a characteristic dimensional length scale of z_0 to $H/2$, and the subsequent reduction in velocity is a consistent feature across all cases studied in this study. This indicates that the emergent current has no memory of the initial height of the intrusion.

It is interesting to note that the reduction in the velocities of the hyperpycnal current does not lead to a relative decrease in the kinetic energy of the system. To see this, we can analyze the domain average kinetic energy ke of the system, defined as

$$ke = \frac{1}{2lh} \int_0^l \int_0^h u^2 + w^2 dx dz. \quad (38)$$

Figure 5 shows the ke for each case with $h = 2$ and different values of Θ . This figure is broken up into two categories for clarity; low Θ ($2.2 \leq \Theta \leq 3$) in Figs. 5(a) and 5(b), and high Θ in Figs. 5(c) and 5(d) ($3 \leq \Theta \leq 8$). Note that T3h2 is included in all four panels. The left column is the entire time history of the ke prior to the current colliding with the end-wall, whereas the right column is the

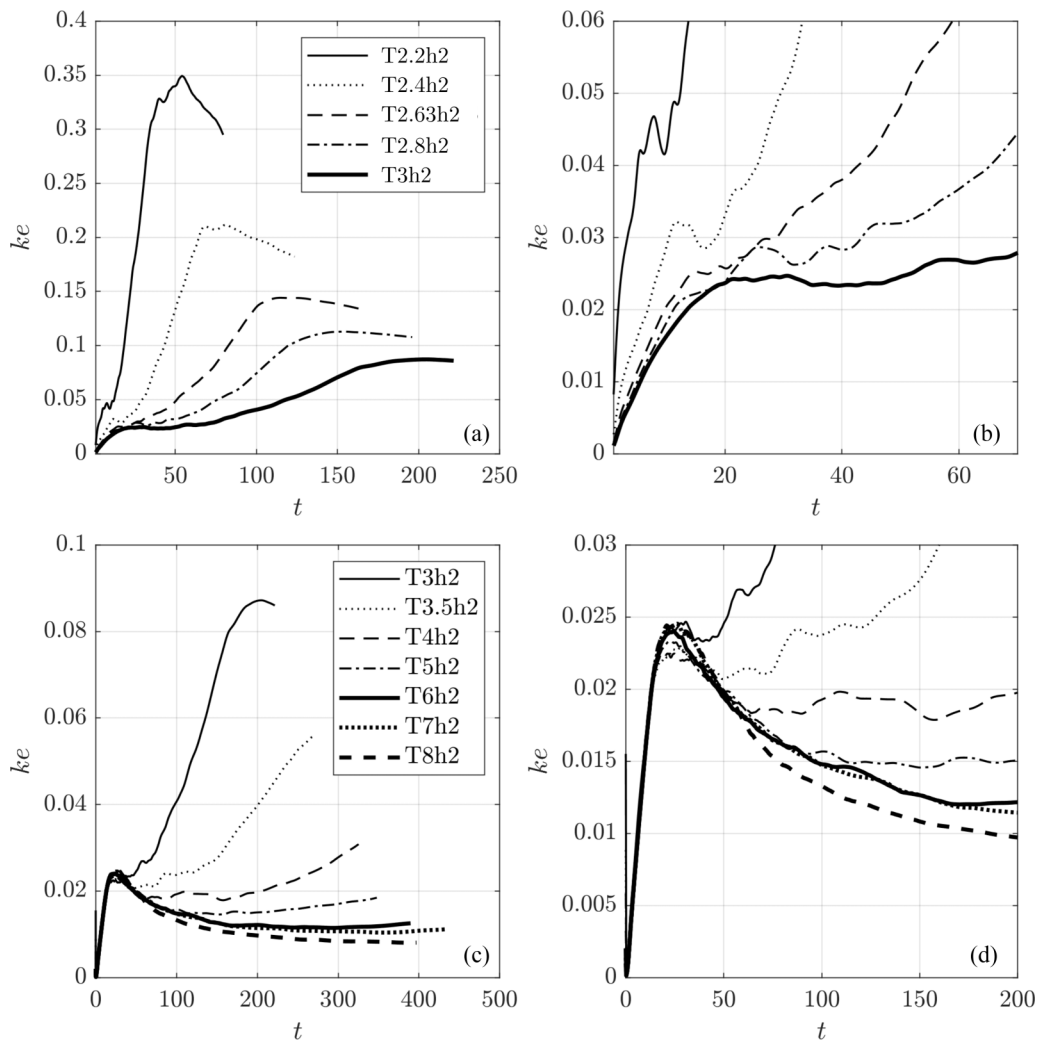


FIG. 5. Time series of the total kinetic energy for all cases with $h = 2$. Panel (a) shows the total kinetic energy for cases with $2.2 \leq \Theta \leq 3$. Panel (c) shows the same quantity for cases with $3 \leq \Theta \leq 8$ (i.e., T3h2 is included on all four plots). Panels (b) and (d) are detailed views of the early evolution.

same data with the axis values adjusted to highlight the early development. Also note the difference in vertical and horizontal scales in each panel. Broadly speaking the evolution of the ke takes place over several stages; an increase by the propagation of the initial hypopycnal current, and an increase in ke by the hyperpycnal current. It should be noted that cabbeling itself is not a source of kinetic energy, but instead increases the potential energy, which is then transformed into kinetic energy by a buoyancy flux. The low Θ cases (T2.2h2, T2.4h2, T2.63h2, T2.8h2, and T3h2) are shown in Figs. 5(a) and 5(b), and these cases are characterized by a short time increase of ke as the initial hypopycnal current propagates, but this is quickly swamped by a much larger increase from the hyperpycnal current. There is a transient period between these stages where the ke oscillates but does not significantly increase. As Θ becomes larger, the initial rate of growth of the ke slows, and the second stage occurs at a later time. Eventually, the total ke reaches a peak and then decreases before the gravity currents ultimately collide with the right-hand wall (the time at which the curves terminate).

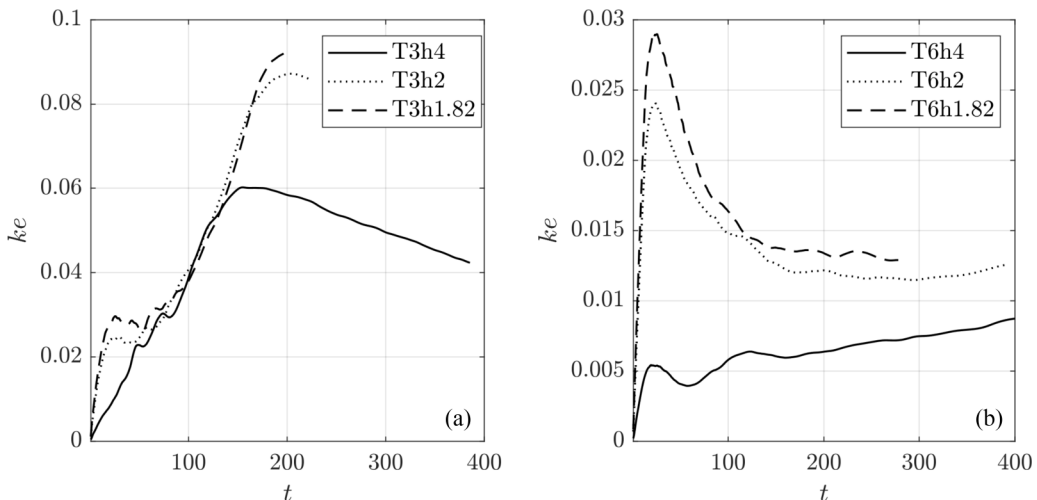


FIG. 6. Time series of the total kinetic energy comparing between cases with varying h (Θ held constant in each panel). Panel (a) shows the cases with $\Theta = 3$, and panel (b) shows the cases with $\Theta = 6$.

We can see in Figs. 5(c) and 5(d) that by further increasing Θ in the 3.5–8 range (T3.5h2, T4h2, T5h2, T6h2, T7h2, and T8h2), the first stage of growth by the propagation of the initial hypopycnal current is elongated resulting in a clear localized peak in the ke , before slowly decreasing as the hypopycnal current spreads. Following this, there is a more gradual increase due to the slumping of the hyperpycnal current. Note that T3h2 is included on all four panels of Fig. 5 as it is an approximate transition between the two kinetic energy evolution regimes. The general behavior that can be gleaned from Fig. 5 is that for Θ near 2, the hypopycnal current does not complete its initial acceleration before cabbeling and the subsequent formation of the hyperpycnal current starts to dominate the kinetic energy history. Conversely, for larger values of Θ , the initial hypopycnal current is allowed to develop into a more mature current before cabbeling ultimately generates the hyperpycnal current. This suggests that the transition occurs because of a competition between two timescales. The first is the cabbeling timescale (the time required for significant dense fluid to be formed due to cabbeling) versus the timescale of propagation of the hypopycnal current. As we increase Θ , we also increase the speed of the current [defined in Eq. (10)], so presumably, the hypopycnal current goes through its natural evolution in a shorter amount of time relative to the cabbeling timescale.

In Fig. 6 we compare the total kinetic energy of two values of Θ (3 and 6) for three values of h . These Θ values were chosen to best illustrate the sensitivity of the total kinetic energy based on the variation of Θ and h . Figures 6(a) and 6(b) show the total kinetic energy for the T3h4, T3h2, and T3h1.82 cases. It is clear that by making the domain shallower (or alternatively increasing the initial intrusion height), we get a more well-defined early evolution of the flow, indicated by the rapid rise and peak in kinetic energy. T3h4 shows a severe early and late reduction in total kinetic energy relative to the T3h2 and T3h1.82 cases, potentially indicating the impact of viscosity due to the relatively low value of Gr . It is interesting that in the interval $100 < t < 200$, the relative increase in the total kinetic energy is similar between T3h4, T3h2, and T3h1.82. This indicates that the development of the hyperpycnal current may be unaffected by the magnitude of Gr over this time interval. Figures 6(c) and 6(d) show the same quantity for cases T6h4, T6h2, and T6h1.82. We can see a better defined initial acceleration of the current, and peak in the kinetic energy. Note that the hyperpycnal currents for T6h2 and T6h1.82 become large enough that they run into the wall at $x = l$ before they can fully develop, but T6h4 does not. This is interesting as the ke increase due to the hyperpycnal current results in a larger total ke than that of the initial peak.

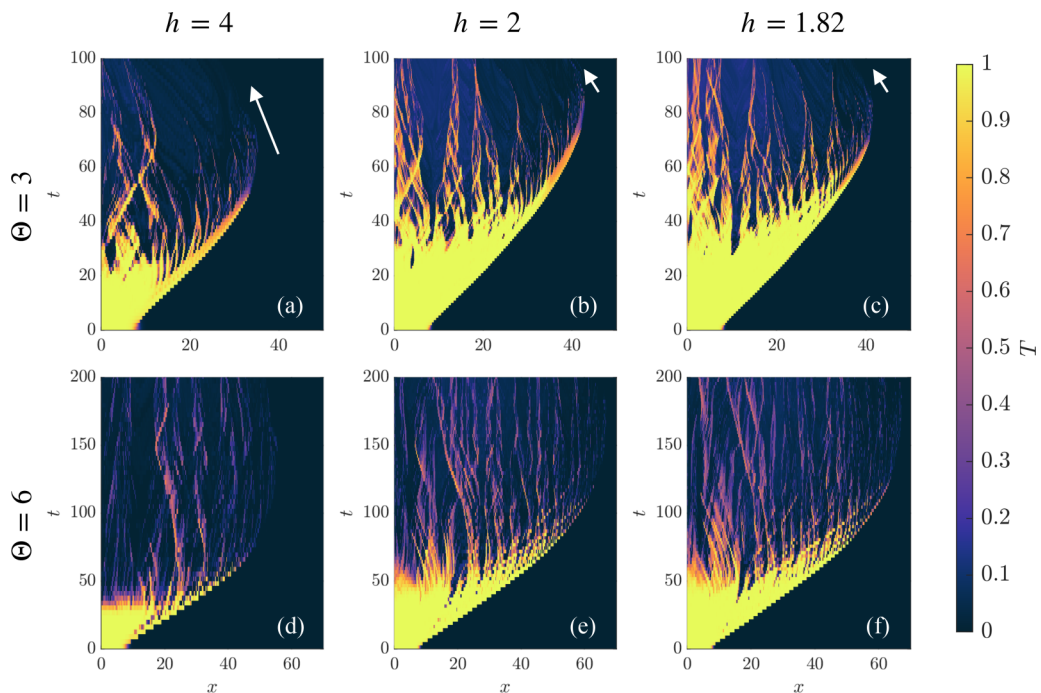


FIG. 7. Hovmoller plots of the temperature at a height of $0.95h$ for the cases with varying Θ and h . Θ is constant along each row of panels, and h is constant along each column. Arrows are included in panels (a), (b), and (c) to highlight the flow reversal.

Figure 6 also serves to show some of the Gr dependence of the flow. Figure 6(a) highlights that by increasing the Grashof number, the early development of the flow (the first local maximum due to the hypopycnal current around $t = 50$) becomes more well-defined (i.e., there is some clear separation between the development of the early peak in ke and the second larger peak due to the hyperpycnal current). Furthermore, it is clear from Fig. 6(b) that the early evolution of the flow that both the maximum ke due to the hypopycnal current is higher for larger Grashof number (smaller h). Additionally, the timescale of the secondary hyperpycnal is longer for larger Grashof number as well.

Figures 7(a)–7(c) show Hovmoeller plots of the temperature field at $0.95h$ for T3h4, T3h2, and T3h1.82 between $0 < x < 50$ and $0 < t < 100$. Figures 7(d)–7(f) shows the same for T6h4, T6h2, and T6h1.82 between $0 < x < 70$ and $0 < t < 200$. These figures highlight the overall similarity in the time history of the near-surface temperature for each of the cases compared. For example, first consider Figs. 7(a)–7(c) [the same discussion below can be applied to Figs. 7(d)–7(f)]. Note that while the broad features such as the propagation speed of the current (inferred by the slope in x - t space of the front) and halting behavior are similar between all three of these cases, T3h4 [shown in Fig. 7(a)] travels the shortest nondimensional distance relative to T3h2 [Fig. 7(b)] and T3h1.82 [Fig. 7(c)], indicating the impact of the low value of Gr . Directly comparing Figs. 7(b) and 7(c) (where Gr has been increased by decreasing h) reveals negligible differences between the distance traveled between these two cases. In other words, there are noticeable differences in the traveled distance between T3h4 and T3h1.82, but comparatively small differences in the traveled distances between T3h2 and T3h1.82. These results indicate that for low enough Grashof number, the quantitative current characteristics are modified relative to cases with higher values Gr . The implication then becomes that the large-scale behavior of the current may be relatively independent of Gr for large enough values. The exact regime where the gravity current evolution achieves Gr

independence is beyond the scope of this study. Some discussion on this is provided in Härtel *et al.* [14] and Cantero *et al.* [37]. Recall that Gr independence in head location was noted in the results of Fig. 5(c) in Grace *et al.* [19], where a larger value of Gr led to an increased discrepancy between the head locations of near-surface propagating currents versus near-bottom propagating currents, and by reducing Gr, these differences became smaller.

Additionally, late in the time history, we can see a near-surface reversal of the propagation direction. The prominence of this feature increases as $\Theta \rightarrow 2$ and was clearly visible in cases where $2 < \Theta < 3$. However, a key feature that these figures highlight is the variation in the maximum extent that the current achieves as Θ is increased for constant h . At low Θ , the current's near-surface forward motion ceases much earlier in the tank relative to a case with larger Θ , made apparent by comparing the horizontal axis across panels in the same column of Fig. 7. This is discussed in the next section.

B. The maximum extent of the current

Figure 7 highlights the propensity of the hypopycnal currents to progress down the length of the domain, and then halt. The maximum distance over which this occurs, denoted by \mathcal{L} , is an important parameter because it represents the length (in the x direction) of the rectangular region that characterizes the volume of fluid that makes up the emergent hyperpycnal current. In a field study, this parameter could be compared to the measured location of the plunging point in an outflow adjacent to a nuclear power plant, for example. For context, the maximum extent of gravity currents has been studied before, but in the context of sediment-laden gravity currents. Maxworthy [38] used laboratory experiments to first identify the formation of a secondary current that flows along the bottom of the domain. He tracked the maximum extent as a function of the excess density ratio (the ratio of density differences due to salt versus that of sediment). Sutherland *et al.* [33] went a step further and performed laboratory experiments of hypopycnal flows that underwent convective sedimentation with varying particle sizes. They measured the maximum distance of the hypopycnal current and found a semi-empirical relationship to the particle diameter. They found that as particles became larger, the maximum extent of the hypopycnal current increased. Davarpanah Jazi and Wells [34] performed experiments along a flat bottom tank and highlighted the expected maximum extent for different intervals of the density ratio.

There has been limited laboratory scale work focused directly on cabbelling gravity currents since precise temperature control in a laboratory environment is practically challenging. However, there are known alternatives that yield the same basic behavior. Experiments featuring a methanol and ethylene glycol (MEG) mixture flowing into a fresh ambient were performed in Huppert *et al.* [39]. By controlling the concentration of methanol, the resulting relationship between the density and concentration of MEG becomes approximately quadratic, allowing for a density maximum to occur when the fresh ambient is mixed with MEG. Several experiments highlighting the evolution of continuous source MEG gravity currents (a simple model representing a pyroclastic cloud) on slopes of 15° and 30° were performed, and their results indicated that as the gravity currents flowed along the sloped roof, entrainment of the ambient caused a dense mixture to form and to sink to the bottom. Their results, while qualitative on the whole, showed empirically that the head locations tend to scale approximately as $t^{0.62}$, with the total distance of the initial current being proportionally to the Reynolds number defined by the nozzle diameter and inflow speed. However, these experiments did not comment on the run-out length of the initial intrusions. Following this, Woods and Bursik [40] performed a systematic study of the angle dependence of the system and found that as the slope of the roof increased, more ambient fluid was entrained, leading to earlier lift-off and a resulting shorter run-out length of the initial intrusion. The critical angle was about 25° , and for slopes less than this critical value, the run out was positively correlated with the angle of the slope, more or less agreeing with the findings of Huppert *et al.* [39].

The point is that in these studies, the maximum extent of the current driven by convective sedimentation in the case of the sediment laden experiments, or the mixing and lofting in the MEG

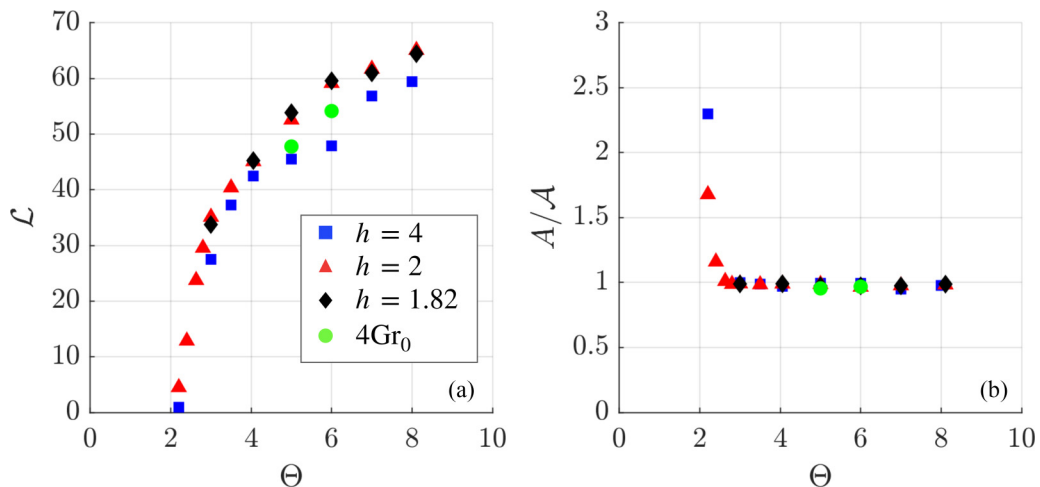


FIG. 8. Panel (a) shows the variation of \mathcal{L} for the large intrusion cases (\blacklozenge), the medium intrusion cases (\blacktriangle), and the small intrusion cases (\blacksquare). VT5h4 and VT6h4 are also included and denoted by \bullet . Panel (b) shows the area of the hyperpycnal current normalized by the area of the entrainment zone \mathcal{A} after the cabbeling is quenched.

experiments is important because it predicts the length scale where one might be concerned about transport of material. More on the significance of the maximum extent in this context can be found in the discussion section. In the simulations presented within this study, it is not necessarily sediment deposition that is of interest, but more the transport of heat (and perhaps dissolved gases in a field setting, for example).

For the following section, we will define

$$\mathcal{L} = f(\Theta, h, Gr_0). \quad (39)$$

We calculate \mathcal{L} by simply recording the location of the front of the gravity current at a height $0.95h$. The location of the front of the gravity current at a given time is defined as the farthest distance from the left-hand wall where $T = T_c$, where $T_c = 0.01$. The computed values for \mathcal{L} are not strongly dependent on the choice of T_c until it is greater than about 0.5 (the estimate of the front location of the current is incorrect) or until it is less than about 0.0001 (small numerical variations in the flow start to give incorrect results). Note that T_c corresponds to a different dimensional temperature for each case.

\mathcal{L} is plotted as a function of Θ in Fig. 8(a). Cases with $h = 4$ are represented by blue squares, cases with $h = 2$ are represented by red triangles, and cases with $h = 1.82$ are represented by black diamonds. VT5h4 and VT6h4 are represented by green circles. We can see that \mathcal{L} generally increases with Θ , however, past $\Theta = 3$ the slope of increase is shallower. Furthermore, for large h (a relatively deep domain), we can see that the maximum extent is severely affected for Θ between 3 and 7, relative to the cases with smaller h . This was also apparent in the temperature Hovmoeller plot in Fig. 7(a). It is not until Θ is increased past about 6 where the maximum extent is more comparable to the cases with $h = 2$ and $h = 1.82$. The reason for this discrepancy is that the Grashof number is small enough that the hypopycnal current enters the viscous regime early in its development, leading to a decreased maximum horizontal extent. This is confirmed by rerunning cases T5h4 and T6h4 but reducing the viscosity by a factor of two (recall that these cases are VT5h4 and VT6h4). Note that by increasing Gr_0 by a factor of four (reducing viscosity by a factor of two), we increase the maximum extent of those two cases. This led to \mathcal{L} values more comparable to the cases with larger h (and equal Θ).

We can see that continuing to increase Θ increases the distance in which the hypopycnal current travels before it halts. As discussed previously, continually increasing Θ implies that the leading order functional form of the buoyancy forcing is purely quadratic, which precludes cabbeling (and similar to the ‘‘T cases’’ presented in Grace *et al.* [19]). For this reason, we should expect \mathcal{L} to continue increasing with Θ but at a slower rate at larger Θ .

The maximum horizontal extent \mathcal{L} is an important parameter because it helps characterize the approximate area of the hyperpycnal current, which consists of mixed ambient and intruding fluid. For each hyperpycnal current, we estimate the area by assuming that the mixing of the hypopycnal current and ambient occurs over a rectangular region of length $\mathcal{L} + x_\ell$, and the depth h . This can be thought of as the ‘‘initial area’’ for the hyperpycnal flow, and for brevity, this region will be called the ‘‘entrainment zone.’’ The full depth is chosen as the vertical length scale since the mixing takes place over the entire depth of the domain. Mathematically, area of the entrainment zone is given by

$$\mathcal{A} = (\mathcal{L} + x_\ell)h. \quad (40)$$

The area of the current calculated from the simulation data at a given time is

$$A = \int_0^l \int_0^h \chi \, dx \, dz, \quad (41)$$

where the indicator function χ is

$$\chi = \begin{cases} 1 & T > T_c \\ 0 & T \leq T_c \end{cases}. \quad (42)$$

Recall $T_c = 0.01$ is the critical temperature, which was found to adequately represent the area of the current. The computed area of the current is sensitive to the choice of T_c , and values of T_c greater than about 0.05 tend to underestimate the area of the current. Figure 8(b) shows the area of the hyperpycnal current A normalized by \mathcal{A} . The times were chosen so that the initial hypopycnal current has ceased flowing and significant mixing between the hyperpycnal current and remaining ambient had not occurred. We can see that for larger Θ , A/\mathcal{A} approaches unity, meaning that $\mathcal{L} + x_\ell$ is a good representation of the lock length of the hyperpycnal current. Conversely, it is apparent that for low Θ , \mathcal{A} underestimates the initial fluid area of the hyperpycnal current. The reason for this lies in the near-surface reverse flow mechanism discussed earlier. For low Θ , cabbeling occurs very quickly relative to the propagation of the gravity current, so the bottom current forms and quickly outruns the initial hypopycnal current. The near-surface reverse flow of equal magnitude (but opposite direction) to the bottom current pushes the initial hypopycnal current back towards the left-hand wall. Thus, cabbeling and subsequent mixing takes place in a very narrow region near the left-hand wall, resulting in a relatively small estimate of \mathcal{L} , and therefore \mathcal{A} .

C. Early hyperpycnal current characteristics

The size of the entrainment zone also affects the temperature distribution of the bottom current. Larger entrainment zones lead to mixing with more ambient fluid, so temperatures will be closer to $T = 0$. We can assess the qualitative properties of the gravity current as Θ varies by comparing the current’s spatial structure at a late time when the hypopycnal current has been mixed out. A comparison is presented in Figs. 9(a)–9(d). In this figure the density field is multiplied by 2Θ . This rescaling puts the maximum density at 1 and the density of the ambient at 0. This facilitates an easy comparison between cases. The times were chosen such that the dimensional temperature in every location of the domain falls between the ambient temperature and \tilde{T}_{md} . By increasing Θ , we can see that the volume of the current is larger, in qualitative agreement with the difference in entrainment zone size, and we can also see that the density distribution within each current is qualitatively different. This is especially noticeable in the body and tail of the current for the T2.2h2 [Fig. 9(a)] case when compared to T3.5h2 [Fig. 9(d)].

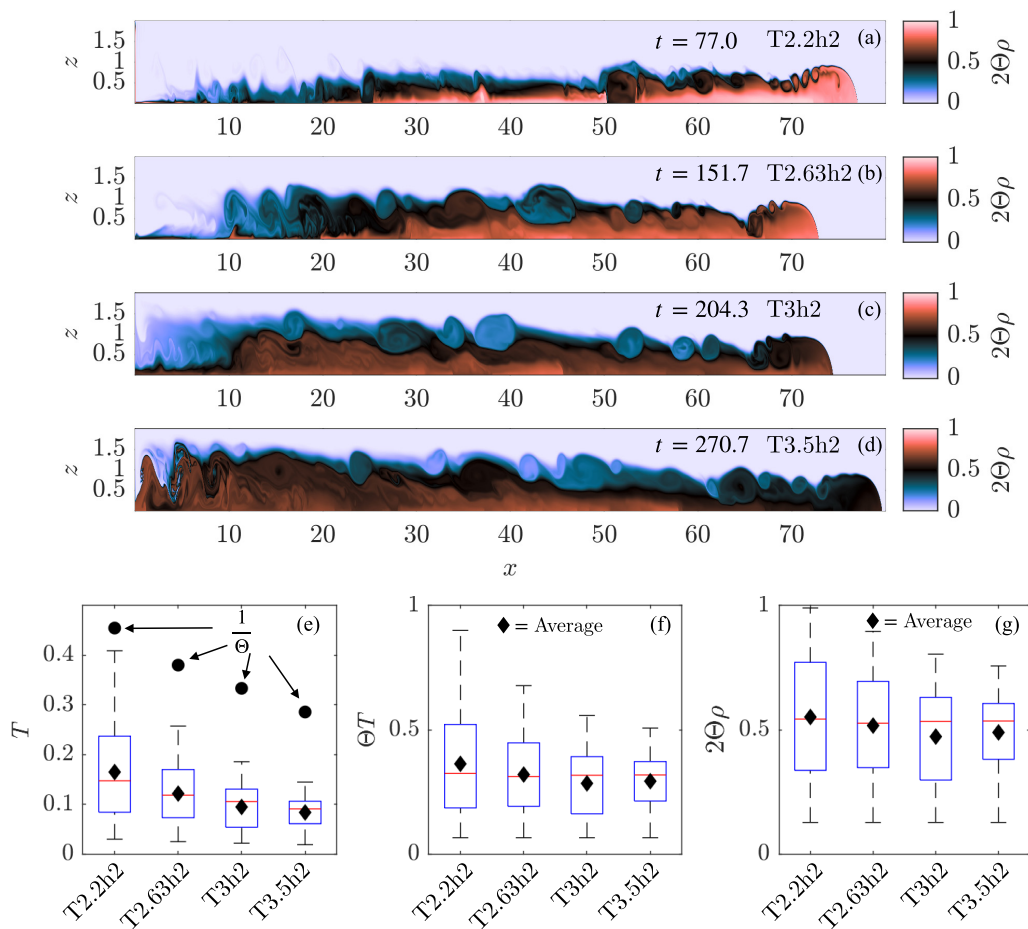


FIG. 9. Panels (a)–(d) show the rescaled density field for several cases. Case names and times are located on the plots. A density of 0 corresponds to the ambient density while a density of 1 corresponds to the maximum density. Panel (e) shows box and whisker plots of the temperature distribution within the current. Panels (f) and (g) show the same data on rescaled axes where 1 corresponds to a temperature $T = \frac{1}{\Theta}$ (the nondimensional temperature of maximum density) and 0 is the ambient temperature. The interquartile range is denoted by the blue boxes and the median temperature is denoted by the red line. The mean temperature of the current is indicated by \blacklozenge and $\frac{1}{\Theta}$ is indicated by \bullet .

Furthermore, the density distribution in the head is clearly different. For lower Θ , the density in the head is much closer to the maximum density (indicated by brighter colors), and increasing Θ tends to decrease the head's density. Along the bottom of the T2.2h2 case, we can see a layer of fluid that is very close to the maximum density, whereas in the T3h2 case, the densities are all less than the maximum density. Since the T3h2 case actually starts with a wider range of temperatures (the largest $\Delta\tilde{T}_1$), it is interesting to note that the temperatures are relatively closer to the ambient. The density fields for the cases with $\Theta > 3.5$ are not shown simply because the tank is not long enough for the hyperpycnal current to develop. In these cases, maximum extent of the hypopycnal current is nearly the entire length of the tank, so the hyperpycnal current simply has no room to develop and propagate.

Figures 9(e)–9(g) provide a measure of the distribution of temperatures within the current for T2.2h2, T2.63h2, T3h2, and T3.5h2. These plots highlight the form of the distribution of

temperatures within the current. The fluid within the current is defined by any parcel that has $T > T_c$. The upper and lower bounds of the blue box indicate the spread between the 25th percentile and 75th percentile of the data, while the upper and lower whiskers show the spread between the lower (upper) extreme and lower (upper) quartile. The horizontal red line represents the median and the filled diamond represents the mean. Figure 9(e) shows the data, as well as the nondimensional temperature of maximum density $\frac{1}{\Theta}$, for the four cases, Fig. 9(f) shows the data on an axis normalized by the temperature of maximum density, and Fig. 9(g) shows the nondimensional density normalized by the maximum density. These plots highlight the fact that by increasing Θ , the distribution of temperatures within the hyperpycnal current become systematically narrower, with the distribution of temperatures grouped around the median. Furthermore, the temperatures become closer to the ambient ($T = 0$). This is further evidence of the general hypothesis that currents with larger Θ mix with a larger volume of ambient fluid, leading to a narrower temperature distribution.

On the other hand, the wider distribution in T2.2h2 is a result of the early evolution of the current. Recall that the formation of the hyperpycnal current occurs relatively early, and this induces the near-surface reverse flow. Thus, the hypopycnal current, which is the source of the cabbeling, reverses direction and is trapped near the left-hand wall, forcing cabbeling only to act in this region. Since the hyperpycnal current continues propagating, dense fluid is fed only to its tail, leading to a wider range of temperature.

An interesting point that is made clear by Fig. 9 concerns the variation of the head location of the currents. We can see that the head location for T3.5h2 is actually the farthest down the length of the tank. The explanation is that the times shown were chosen to best highlight the state of the current after it has begun to flow, and not necessarily to facilitate a comparison in head location. However, this brings up an interesting question about long term evolution of the hyperpycnal currents. As Θ is increased, the head speed of the initial hypopycnal current increases, meaning more distance is covered in the first phase of its evolution over a given time interval. However, for large enough Θ , the area of ambient fluid that is entrained is larger leading to a much smaller density difference between the head of the hyperpycnal current and the remaining ambient, evidenced by Figs. 9(e)–9(g). Thus, while these currents may initially attain larger distances, it is reasonable to think that the hyperpycnal currents from lower Θ cases may eventually catch up due to their larger driving density difference.

IV. SUMMARY AND DISCUSSION

In this study, we performed numerical simulations of gravity currents in the cabbeling regime (cabbeling occurs when two masses of water with temperatures on opposite sides of T_{md} mix and a denser mass of water is generated). By appropriately nondimensionalizing the equations of motion, the NLEOS parameter Θ (the ratio of two characteristic temperature differences) appeared. We highlighted the general evolution of a specific class of gravity currents where $\Theta > 2$, which meant that the density of the ambient was initially closer to the maximum density than the density of the intrusion was. This meant the currents initially rose and flowed along the surface (i.e., a hypopycnal was generated). Mixing between the ambient and intruding fluids led to cabbeling which in turn led to a denser hyperpycnal current that flowed along the bottom surface.

In the present study, both Θ and h (the nondimensional depth) were varied to build an understanding of the general behavior of these currents in (Θ, h) space. In general, we found that currents initially slumped to the top surface and propagated while mixing along the body and tail of the current generated dense water due to cabbeling. Sinking of the dense water continually occurs as the initial hypopycnal current flows and eventually a hyperpycnal current forms along the bottom surface of the domain. This emergent current quickly outruns the initial hypopycnal current. A consistent feature across all cases was that the head height of the hyperpycnal current was about half the depth of the domain, regardless of the initial height of the hypopycnal current. This observation regarding the hyperpycnal current agrees with the theory shown in Linden *et al.* [18], who showed with the use of an energy conservation argument that the head height of the current must be half

its lock release depth. Thus, the “effective lock release depth” of the hyperpycnal current is H , the depth of the domain.

To further categorize the behavior of these currents, we considered the domain average kinetic energy, denoted by ke , and found that as Θ was increased, the timescale of the development of the gravity current increased before the onset of cabbeling. This agrees with the perturbation analysis that showed cabbeling became less important to the dynamics in the limit of large Θ . Computing ke also showed that decreasing the height of the initial water mass led to a relatively small increase in kinetic energy due to cabbeling at constant Θ . By using the near-surface temperature in the along-tank direction, the maximum horizontal extent, \mathcal{L} of each current was also tracked and compared. We showed that as Θ increases, the maximum extent of the hypopycnal current increased as well, but the slope decreased as Θ became larger. Increasing h led to a reduction in horizontal extent at constant Θ . The Grashof number for the high h cases was small enough that viscous effects played a significant role early on. This was evident for cases T3h4, T4h4, and T5h4, as \mathcal{L} clearly scales differently than the cases with $h = 2$ and $h = 1.82$. Two simulations were performed where the Grashof number was modified by changing viscosity (VT5h4 and VT6h4). By changing the value of viscosity, we can change the value of the Grashof number but keep Θ and h unchanged. In these cases the viscosity was reduced by 50% leading to an increase in the Grashof number by a factor of four. This led to larger maximum extents relative to the comparable cases T5h4 and T6h4. Similar behavior was seen in experiments by Gladstone *et al.* [41], as well as Grace *et al.* [19].

We used the maximum extent of the current as well as the total depth to define a rectangular region called the entrainment zone. This region acts as the reservoir of fluid that makes up the hyperpycnal current. It was shown that the entrainment zone is a good indicator of the area of fluid that makes up the hyperpycnal current except for Θ near two. In this regime, the calculated entrainment zone underestimated the volume of the hyperpycnal current. For Θ close to two, the timescale for cabbeling was found to be shorter than the timescale of initial propagation of the current, so cabbeling occurred quickly and the hyperpycnal current formed before the initial hypopycnal current propagated a significant distance.

The distribution of density and temperature of the hyperpycnal current was also studied. The key observation is that increasing Θ makes the distribution of temperatures narrower about the median temperature. As Θ was increased, the hypopycnal current mixed with a larger region of ambient fluid, leading to an average temperature of the mixture closer to the temperature of the ambient. Alternatively, by reducing Θ to be close to two, the distribution was found to be wider, with more locations within the flow being close to $\frac{1}{\Theta}$ (the nondimensional temperature of maximum density). Thus, hyperpycnal currents with Θ close to two generally exhibited more regions of dense fluid than currents with larger Θ .

The results of this study highlight an important characteristic about gravity currents. For a sufficiently large Reynolds number, gravity currents go through several self-similar phases of evolution as they progress, each corresponding to a different dominant momentum balance within the current. These phases are called the acceleration phase, the slumping phase, the inertial phase, and the viscous phase. In the acceleration, slumping and inertial phases, the dominant balance is between the driving pressure gradient generated by density differences, and the inertial term in the momentum equations. In the viscous phase, the dominant balance is instead between the inertial term and the viscous term. Each of these four phases manifest themselves as (among other things) a different scaling law for the head speed of the current. Cantero *et al.* [37] discusses each of the four phases and provides evidence for the dominant balance within each phase. They also provide quantitative relationships between the head speed, time, and the normalized lock-release volume V_0 . For example, in the slumping phase, the gravity current head speed is approximately independent of time, and the time the current spends in this regime is simply proportional to V_0 . In this regime, density changes within the head, as well as head height changes are negligible. It is not until the inertial regime, where the head speed scales as $V_0^{1/3}$ that gravity currents experience more significant head height and density changes.

How might we apply these regimes to the hypo- and hyperpycnal currents presented in this study? We expect that the only circumstance in which the currents may progress through these phases is in the high Θ limit. A primary assumption of the theory of each phase is that the volume of the current does not deviate strongly from its initial value [17], and since the initial hypopycnal currents with low Θ are immediately disrupted by cabbeling, this assumption is not satisfied. However, in the high Θ limit, we saw that the leading order behavior was that of a noncabbeling gravity current, so there is potential that currents in this limit may progress through each phase before cabbeling can completely extract the intruding fluid. More work is necessary to fully characterize these currents. Furthermore, as we saw in Grace *et al.* [19] in Fig. 5(a), the head speed does not necessarily scale with time in the same way under a nonlinear equation of state.

The more pertinent question is regarding the hyperpycnal current. As we saw, varying Θ increased the size of the entrainment zone, and the resulting hyperpycnal current. In principle, one can expect that increasing Θ indirectly increases the time interval of each of these regimes for the hyperpycnal current by increasing the nominal lock length, and therefore the V_0 . What complicates this is the fact that by increasing Θ , we increase the initial volume of entrained ambient fluid, which reduces the characteristic density difference between hyperpycnal current and the remaining ambient. This is evident by the smaller mean and median temperatures and densities shown in Fig. 9(b). This density difference affects the buoyancy velocity and therefore the nondimensional timescales on which the gravity current flows. A point of future work could be to make a more comprehensive characterization of the hyperpycnal current characteristics, such as a quantifying whether the phenomenological lock length can compensate for the reduced timescales created by the mixing, resulting in a net increase in the horizontal transport of heat and material with increasing Θ .

There are several additional future directions to take this research. Are the results of this study significantly affected by three-dimensionality? Vortex tilting and stretching may enhance the rate of mixing when compared to two-dimensional simulations. Could this affect the rate that the hypopycnal currents mix with the ambient? If mixing occurs more rapidly over the course of hypopycnal current evolution, there may be implications for the rate of formation and the characteristics of the hyperpycnal current. If mixing happens more rapidly and more efficiently, the hyperpycnal current temperature distributions may be narrower and their mean temperature may be farther from the ambient, due to there being a smaller volume of entrained ambient fluid. This could allow a three-dimensional hyperpycnal current to travel farther than a comparable two-dimensional case.

Furthermore, for readers more interested in turbulent structures, the simulations presented in this study could be rerun in three dimensions at large Gr [see (14)]. It has been shown that turbulent structures in the tail of a gravity current have some impact on the head location and head speed of the current late in its evolution. Cantero *et al.* [37] and references within discussed this impact and found that when simulating gravity currents in two dimensions, two-dimensional coherent vortical structures in the tail of the current led to a reduction in the driving pressure gradient of the flow. They compared these results to three dimensional cases at the same Reynolds number and found that the pressure reduction within the tail was weaker for the three-dimensional cases. This led to a larger head speed in the inertial and viscous regimes for the three-dimensional cases compared to the two-dimensional cases. Thus, how might the evolution of the hypopycnal current be affected by three-dimensionality within the tail region of the current?

Last, we should identify if the relationship between \mathcal{L} , Θ , and h is substantially different if the boundary conditions are changed to no-slip. In the high Gr limit, we should expect that the boundary layers are significantly thinner relative to the length scales of the interior flow, so the interior should evolve similar to the results presented here. However, it is unclear on if no-slip boundary conditions are even the “correct” boundary conditions. One could think that a density driven flow might be flowing beneath ice, so the boundary conditions have a certain variable roughness associated with them, as well as thermal boundary layers, melting (especially for high Θ), and entrainment of melt water. Furthermore, if these currents flow along the an open water surface, the significant role that wind and surface waves play in the evolution of subsurface currents must be included.

ACKNOWLEDGMENTS

This work was supported by a grant from Global Water Futures, funded by the Canada First Research Excellence Fund, and from the Canadian Foundation for Innovation and the Ontario Research Fund. This research was also enabled in part by support provided by SHARCNET and the Digital Research Alliance of Canada. The authors also gratefully acknowledge Bertram Boehrer, Michael Waite, Jean-Pierre Hickey, and Chris Fletcher for constructive feedback on early versions of this manuscript. The authors would also like to thank the two anonymous reviewers whose suggestions and criticisms have led to substantial improvements to this paper.

-
- [1] S. M. Powers and S. E. Hampton, Winter limnology as a new frontier, *Limnol. Oceanogr. Bull.* **25**, 103 (2016).
 - [2] G. Kirillin, M. Leppäranta, A. Terzhevik, N. Granin, J. Bernhardt, C. Engelhardt, T. Efreanova, S. Golosov, N. Palshin, P. Sherstyankin, G. Zdrovennova, and R. Zdrovennov, Physics of seasonally ice-covered lakes: A review, *Aquatic Sci.* **74**, 659 (2012).
 - [3] J. Jansen, S. MacIntyre, D. C. Barrett, Y.-P. Chin, A. Cortés, A. L. Forrest, A. R. Hryciuk, R. Martin, B. C. McMeans, M. Rautio, and R. Schwefel, Winter limnology: How do hydrodynamics and biogeochemistry shape ecosystems under ice? *J. Geophys. Res.: Biogeosci.* **126**, 1 (2021).
 - [4] B. Boehrer and M. Schultze, Stratification of lakes, *Rev. Geophys.* **46**, RG2005 (2008).
 - [5] T. D. Foster, An analysis of the cabbeling instability in sea water, *J. Phys. Oceanogr.* **2**, 294 (1972).
 - [6] T. D. Foster and E. C. Carmack, Temperature and salinity structure in the Weddell Sea, *J. Phys. Oceanogr.* **6**, 36 (1976).
 - [7] T. J. McDougall, Thermobaricity, cabbeling, and water-mass conversion, *J. Geophys. Res.* **92**, 5448 (1987).
 - [8] S. Groeskamp, R. P. Abernathey, and A. Klocker, Water mass transformation by cabbeling and thermobaricity, *Geophys. Res. Lett.* **43**, 10,835–10,845 (2016).
 - [9] C. J. Shakespeare and L. N. Thomas, A new mechanism for mode water formation involving cabbeling and frontogenetic strain at thermohaline fronts. Part II: Numerical simulations, *J. Phys. Oceanogr.* **47**, 1755 (2017).
 - [10] J. E. Simpson, Gravity currents in the laboratory, atmosphere, and ocean. *Annu. Rev. Fluid Mech.* **14**, 213 (1982).
 - [11] J. E. Simpson, *Gravity Currents: In the Environment and the Laboratory*, 2nd ed. (Cambridge University Press, Cambridge, 1999).
 - [12] M. G. Wells and R. M. Dorrell, Turbulence processes within turbidity currents, *Annu. Rev. Fluid Mech.* **53**, 59 (2021).
 - [13] E. Meiburg and B. Kneller, Turbidity currents and their deposits, *Annu. Rev. Fluid Mech.* **42**, 135 (2010).
 - [14] C. Härtel, F. Carlsson, and M. Thunblom, Analysis and direct numerical simulation of the flow at a gravity-current head. Part 2. The lobe-and-cleft instability, *J. Fluid Mech.* **418**, 213 (2000).
 - [15] C. Härtel, E. H. Meiburg, and F. Necker, Analysis and direct numerical simulation of the flow at a gravity-current head. Part 1. Flow topology and front speed for slip and no-slip boundaries, *J. Fluid Mech.* **418**, 189 (2000).
 - [16] R. Ouillon, E. Meiburg, and B. R. Sutherland, Turbidity currents propagating down a slope into a stratified saline ambient fluid, *Environ. Fluid Mech.* **19**, 1143 (2019).
 - [17] H. E. Huppert and J. E. Simpson, The slumping of gravity currents, *J. Fluid Mech.* **99**, 785 (1980).
 - [18] P. Linden, Gravity currents - theory and laboratory experiments, *Buoyancy-Driven Flows*, edited by E. Chassignet, C. Cenedese, and J. Verron, Vol. 13 (Cambridge University Press, Cambridge, 2012), Chap. 1, p. 51.
 - [19] A. P. Grace, M. Stastna, K. G. Lamb, and K. A. Scott, Asymmetries in gravity currents attributed to the nonlinear equation of state, *J. Fluid Mech.* **915**, A18 (2021).

- [20] K. D. Stewart, T. W. N. Haine, A. McC. Hogg, and F. Roquet, On cabbeling and thermobaricity in the surface mixed layer, *J. Phys. Oceanogr.* **47**, 1775 (2017).
- [21] E. C. Carmack, Combined influence of inflow and lake temperatures of spring circulation in a riverine lake, *J. Phys. Oceanogr.* **9**, 422 (1979).
- [22] E. C. Carmack, B. J. Gray, H. Pharo, and R. J. Daley, Importance of lake-river interaction on seasonal patterns in the general circulation of Kamloops Lake, British Columbia, *Limnol. Oceanogr.* **24**, 634 (1979).
- [23] P. R. Holland and A. Kay, A review of the physics and ecological implications of the thermal bar circulation, *Limnologica* **33**, 153 (2003).
- [24] M. N. Shimaraev, N. G. Granin, and A. A. Zhdanov, Deep ventilation of Lake Baikal waters due to spring thermal bars, *Limnol. Oceanogr.* **38**, 1068 (1993).
- [25] M. Schmid, N. M. Budnev, N. G. Granin, M. Sturm, M. Schurter, and A. Wüest, Lake Baikal deepwater renewal mystery solved, *Geophys. Res. Lett.* **35**, L09605 (2008).
- [26] G. Kirillin, T. Shatwell, and P. Kasprzak, Consequences of thermal pollution from a nuclear plant on lake temperature and mixing regime, *J. Hydrol.* **496**, 47 (2013).
- [27] A. Gaudard, C. Weber, T. J. Alexander, S. Hunziker, and M. Schmid, Impacts of using lakes and rivers for extraction and disposal of heat, *WIREs Water* **5**, 1 (2018).
- [28] B. O. Tsydenov, A. Kay, and A. V. Starchenko, Numerical modeling of the spring thermal bar and pollutant transport in a large lake, *Ocean Model.* **104**, 73 (2016).
- [29] D. C. Wilcox, Reassessment of the scale-determining equation for advanced turbulence models, *AIAA J.* **26**, 1299 (1988).
- [30] S. B. Pope, *Turbulent Flows* (Cambridge University Press, Cambridge, 2000).
- [31] P. R. Holland, A. Kay, and V. Botte, A numerical study of the dynamics of the riverine thermal bar in a deep lake, *Environ. Fluid Mech.* **1**, 311 (2001).
- [32] C. J. Subich, K. G. Lamb, and M. Stastna, Simulation of the Navier-Stokes equations in three dimensions with a spectral collocation method, *Int. J. Numer. Methods Fluids* **73**, 103 (2013).
- [33] B. R. Sutherland, M. K. Gingras, C. Knudson, L. Steverango, and C. Surma, Particle-bearing currents in uniform density and two-layer fluids, *Phys. Rev. Fluids* **3**, 023801 (2018).
- [34] S. Davarpanah Jazi and M. G. Wells, Dynamics of settling-driven convection beneath a sediment-laden buoyant overflow: Implications for the length-scale of deposition in lakes and the coastal ocean, *Sedimentology* **67**, 699 (2020).
- [35] J. Olsthoorn, E. W. Tedford, and G. A. Lawrence, Diffused-interface Rayleigh-Taylor instability with a nonlinear equation of state, *Phys. Rev. Fluids* **4**, 094501 (2019).
- [36] A. P. Grace, M. Stastna, K. G. Lamb, and K. A. Scott, Numerical simulations of the three-dimensionalization of a shear flow in radiatively forced cold water below the density maximum, *Phys. Rev. Fluids* **7**, 023501 (2022).
- [37] M. I. Cantero, S. Balachandar, M. H. García, and D. Bock, Turbulent structures in planar gravity currents and their influence on the flow dynamics, *J. Geophys. Res.: Oceans* **113**, C8 (2008).
- [38] T. Maxworthy, The dynamics of sedimenting surface gravity currents, *J. Fluid Mech.* **392**, 27 (1999).
- [39] H. E. Huppert, J. S. Turner, S. N. Carey, R. S. J. Sparks, and M. A. Hallworth, A laboratory simulation of pyroclastic flows down slopes, *J. Volcanol. Geotherm. Res.* **30**, 179 (1986).
- [40] A. W. Woods and M. I. Bursik, A laboratory study of ash flows, *J. Geophys. Res.* **99**, 4375 (1994).
- [41] C. Gladstone, L. J. Ritchie, R. S. J. Sparks, and A. W. Woods, An experimental investigation of density-stratified inertial gravity currents, *Sedimentology* **51**, 767 (2004).